Magnetic Resonance Electrical Properties Tomography (MREPT)

8

Ulrich Katscher, Atul Singh Minhas, and Nitish Katoch

Abstract

This chapter explains the magnetic resonance electrical impedance tomography (MREPT) technique used to image electrical properties at high frequencies. The chapter describes the MREPT data acquisition methods, current state-of-the-art image reconstruction algorithms, and experiments with phantoms, animals, and humans.

8.1 Introduction

Magnetic resonance electrical properties tomography (MREPT) is a technique to measure the electrical properties (EPs) of body tissues, such as electrical conductivity and permittivity, at the Larmor frequency of MRI. For example, MREPT performed at 3T and 9.4T provides EPs at 128 and 400 MHz, respectively.

8.2 MREPT Data Acquisition

Unlike MREIT or DT-MREIT, MREPT does not require any external current to map EPs. Instead, the reconstruction of EPs relies on the knowledge of the complex RF transmit (TX) field $B_1 = |B_1|e^{i\phi}$, given by its amplitude $|B_1|$ (corresponding to local flip angle α) and phase ϕ. Although these two quantities belong to the same physical field, usually two different MR sequences are applied to measure $|B_1|$ and ϕ, i.e., there is a (large) family of sequences measuring $|B_1|$ (so-called B_1-mapping methods) and another (somewhat smaller) family of sequences measuring ϕ. These two families of pulse sequences are summarized in the Sects. 8.3 and 8.3.2.

The image reconstruction algorithms in EPT involve a second derivative in all three spatial directions (see Sect. 8.4.2), which is the reason why a volumetric data set has to be acquired for EPT. Thus, a single 2D image is not sufficient, but instead a "true" 3D dataset or multiple 2D datasets are required. Multiple 2D datasets are more robust in case of patient motion, however, might suffer from inconsistent sequence calibration between slices, hampering differentiation in

U. Katscher
Philips Research, Hamburg, Germany
e-mail: ulrich.katscher@philips.com

A. S. Minhas (✉)
School of Engineering, Macquarie University, Wallumattagal Campus, Macquarie Park, NSW, Australia
e-mail: atul.minhas@mq.edu.au

N. Katoch
Department of Biomedical Engineering, Kyung Hee University, Seoul, South Korea
e-mail: nitish@khu.ac.kr

R. Sadleir, A. S. Minhas (eds.), *Electrical Properties of Tissues*, Advances in Experimental Medicine and Biology 1380, https://doi.org/10.1007/978-3-031-03873-0_8

through-plane direction. This problem is eliminated by acquiring true 3D datasets.

8.3 Pulse Sequences and Data Processing for B_1 *Magnitude* Measurement

Mapping $|B_1|$ has been investigated since the early days of MR, and over the decades, a large number of these B_1-mapping methods has been developed, independent of EPT. In general, the higher the accuracy of the B_1-mapping method, the better it is for EPT. The accuracy of B_1-mapping methods has been investigated both in general studies without EPT [33] and in EPT [6]. The most popular B_1-mapping methods nowadays appear to be actual flip angle imaging (AFI) [45], Bloch-Siegert shift method (BSS, [35]), and dual refocusing echo acquisition mode method (DREAM, [31]). These methods are briefly described in the following subsections.

AFI

The AFI method [45] uses a steady-state sequence which applies two identical RF pulses followed by two different repetition times TR_1 and TR_2. After each RF pulse, a gradient echo signal is acquired. If TR_1 and TR_2 are sufficiently short and if the transverse magnetization is completely spoiled, the ratio $u(\mathbf{r}) = S_2(\mathbf{r})/S_1(\mathbf{r})$) of the two measured signal intensity distributions $S_1(\mathbf{r})$ and $S_2(\mathbf{r})$ corresponding to TR_1 and TR_2 depends on flip angle $\alpha(\mathbf{r})$ via $v = TR_2/TR_1$:

$$u(\mathbf{r}) = \frac{1 + v\cos\alpha(\mathbf{r})}{v + \cos\alpha(\mathbf{r})} \tag{8.1}$$

and, thus, the spatial distribution of $\alpha(\mathbf{r})$ can be calculated as

$$\alpha(\mathbf{r}) = \arccos\left(\frac{vu(\mathbf{r}) - 1}{v - u(\mathbf{r})}\right). \tag{8.2}$$

BSS

The Bloch-Siegert shift (BSS) is caused by irradiating with an off-resonance RF pulse following conventional spin excitation. When applying the off-resonance RF in the kilohertz range, spin nutation can be neglected, and the primarily observed effect is a spin precession frequency shift. This shift is proportional to the square of the magnitude of B_1. Placing gradient imaging after the off-resonance pulse yields spatially resolved B_1 maps [35]. The phase difference of two acquisitions, with the RF pulse applied at two frequencies symmetrically around the water resonance, is used to eliminate undesired off-resonance effects due to B_0 inhomogeneities and chemical shift. Care has to be taken that occurring SAR (upped by the off-resonance pulses) does not exceed physiologically and legally recommended limits.

DREAM

The dual refocusing echo acquisition mode (DREAM) technique applies a stimulated echo acquisition mode (STEAM) preparation sequence followed by a tailored single-shot low-angle gradient echo train. In contrast to conventional STEAM imaging, both, the stimulated echo and the free induction decay (FID), are refocused quasi-simultaneously as gradient-recalled echoes [31]. In a post-processing step, the actual flip angle of the STEAM preparation RF pulse is derived from the ratio of the two measured signals. Due to this quasi-simultaneous acquisition of the two images (practically all B_1-mapping methods rely in one or the other way on the acquisition of two separate images), DREAM seems to be one of the fastest B_1-mapping methods of all B_1-mapping methods discussed today.

All these B_1-mapping methods would allow to measure absolute values of B_1, which are typically in the range of 5–15 μT. However, the knowledge of absolute values of B_1 is not required for the reconstruction of electrical properties (not even for reconstructing electrical properties quantitatively). It should be noted that it is also irrelevant for EPT to optimize the flip angle or make a careful consideration for calculation of the magnetic field H (unit A/m) and the magnetic flux density B (unit T).

8.3.1 Examples of B_1 *Magnitude* Measurements

The B_1 magnitude obtained using the AFI method is illustrated in Fig. 8.1 for an example phantom and in vivo measurements in the human brain. For each of these experiments, AFI method has been used with a voxel size of $4 \times 4 \times 8$ mm^3, sagittal imaging plane, foldover in anterior/posterior direction, a field of view (FoV) of 224×224 mm^2 in-plane, and 160 mm through-plane. For in vivo experiments, a slight in-plane rotation has been applied such that backfolding from eye motion is placed below the brain. AFI was performed with flip angle = 60^o, TR1 = 30 ms, TR2 = 160 ms, TE = 2.5 ms, and NEX = 1, yielding a total acquisition time of 3:33 min. Afterward, spatial resolution of the B_1 magnitude maps was increased linearly to $1 \times 1 \times 1$ mm^3 to match the spatial resolution of the B_1 phase maps shown in the next Sect. 8.3.2.

8.3.2 Pulse Sequences and Data Processing for B_1 *Phase* Measurement

Mapping of B_1 magnitude, as discussed in the previous section, has been undertaken for decades without having EPT in mind. This is not the case for mapping of B_1 phase ϕ, which became popular only during the last few years specifically with respect to EPT. The main challenge in mapping ϕ is the suppression of phase contributions unrelated to RF penetration [9], particularly phase contributions arising from (a) B_0 inhomogeneities (also called off-resonance effects), (b) patient motion, and (c) eddy currents induced by gradient switching. A direct measurement of ϕ as phase of TX RF field is not possible with a standard MR system. Instead, we have to rely on its superposition with its counterpart, the receive RF field (RX), yielding the so-called transceive (TRX) phase. From this point, ϕ should be interpreted as the TRX phase. This section describes the measurement of the B_1 TRX phase, and its background theory is described in the subsequent section. Three types of sequences are discussed for measuring TRX phase: spin echo (SE)-based sequences, steady-state free precession (SSFP) sequences, and sequences with ultrashort/zero echo time (UTE/ZTE).

We would like to emphasize it as a warning that phase is a very sensitive quantity. While it is a big advantage for EPT to be able to detect even small changes of conductivity, unfortunately it makes phase susceptible to all sorts of artifacts. Even in phantoms, it is very difficult to obtain an artifact-free conductivity map with EPT. This feature has to be kept in mind if acceleration methods like parallel imaging or compressed sensing are applied, which in theory do not change phase and should thus be compatible with EPT phase measurements but in practice may introduce additional artifacts. Note that even small artifacts introduced by these techniques could spoil the reconstruction results.

SE

The easiest way to exclude the unwanted B_0-related phase is to apply spin echo-based sequences, where the refocusing RF pulse eliminates this phase contribution automatically. Since standard SE sequences tend to have excessive acquisition times, particularly for the required volumetric dataset, all kinds of accelerated ("turbo") sequence versions have been applied. Effects of eddy currents from gradient switching can be eliminated by repeating the measurement with inverted gradient polariza-

(continued)

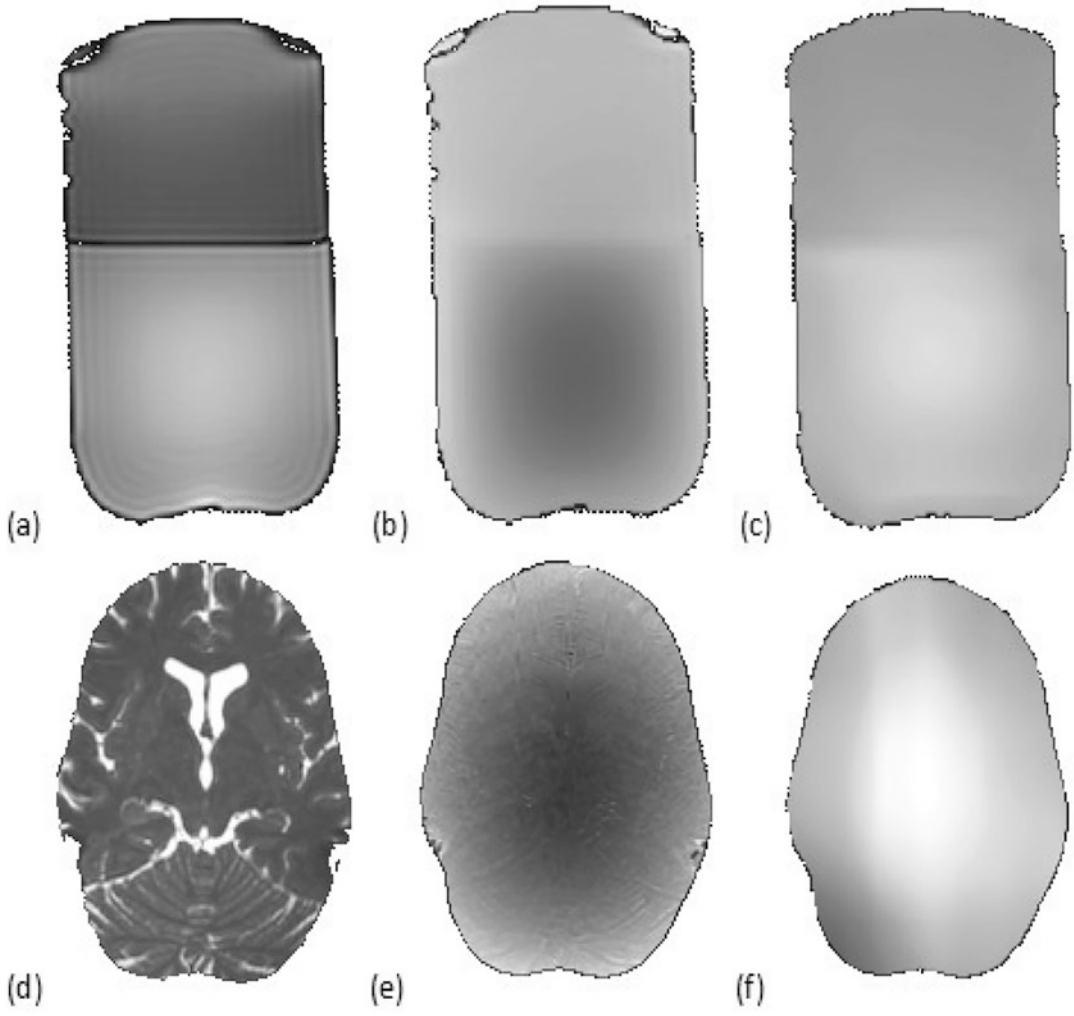

Fig. 8.1 Measurements of phantom and in vivo (axial reformats). Magnitude of SSFP image (**a, d**), transceive phase of SSFP image (**b, e**) taken as B_1 phase, and B_1 magnitude (**c, f**) measured with AFI

tion and averaging the two results (before or after EPT reconstruction) [41]. Effects of patient motion can be suppressed by, e.g., using a double spin echo sequences [4]. For enhanced SNR, multi-spin multi-echo (MSME) can be applied [24], and echoes can be combined by using a method described in [24].

SSFP

Gradient echo sequences contain unwanted B_0-related phase contributions, unless the gradients are balanced over time. Gradients balanced in each of the spatial direction leads to the so-called "steady-state free precession (bSSFP)" sequence. This sequence is very SNR-efficient, robust with respect to motion, shows negligible effect of eddy currents, and thus seems to be the method

(continued)

of choice for determination of ϕ in EPT [39]. The bSSFP sequence is used in the experimental results described in Fig. 8.1 for B_1 phase mapping. However, a major issue is the appearance of banding artifacts, exhibiting signal voids and phase jumps where B_0 inhomogeneities are large for a given TR. Therefore, we must check in each experiment if bSSFP is applicable for the given region of interest and for the given MR system with its individual capability to minimize TR as well as B_0 inhomogeneities. Methods have been reported to eliminate bSSFP banding artifacts (see, e.g., [6]); however, this comes at a cost of (significantly) extended scan duration.

UTE/ZTE

The unwanted phase contribution from B_0 inhomogeneities increases roughly linearly with echo time. Thus, the shorter the echo time, the smaller this unwanted phase contribution. This is the reason why ultrashort or zero echo time (UTE/ZTE) sequences are able to provide a phase which can be used for EPT [21, 37]. Since the SNR of particular tissue types with short relaxation times benefit greatly from ultrashort/zero TE, this idea might become valuable for investigating corresponding tissues like the cartilage or lung [15].

8.3.3 Examples of B_1 *Phase* Measurement

For illustration of B_1 phase mapping with both phantom and in vivo human experiments, a bSSFP sequence has been applied with the geometric setup coinciding with the B_1 magnitude mapping sequence described in Sect. 8.3.1 above. For example, the same location of FOV, sagittal planes, and foldover in anterior/posterior direction was used as that of the AFI method in Sect. 8.3.1 above. However, in vivo FOV was slightly rotated due to backfolding from eye motion, which for B_1 phase mapping typically causes even bigger artifacts than for B_1 magnitude mapping. Sequence parameters were voxel size$= 2 \times 2 \times 2\,\text{mm}^3$, flip angle = 30°, TR = 2.5 ms, TE = 1.2 ms, NEX = 12 for phantom and voxel size$= 1 \times 1 \times 1\,\text{mm}^3$, flip angle = 30°, TR = 3.5 ms, TE = 1.7 ms, and NEX = 2 for in vivo, yielding a total acquisition time of 4:30 min for phantom and 4:10 min for in vivo. SSFP sequences are usually accompanied by very sharp and nasty acoustic noise; thus ear plugs for the volunteer are absolutely necessary.

A commercial 3T scanner (Philips Ingenia, Best, the Netherlands) has been applied for the example scans using a two-channel RF body coil in quadrature mode for RF TX and an eight-channel RF head coil for RF RX (for the described experiments, a single TX channel RF body coil would do as well). The built-in option CLEAR ("constant level of appearance") was used to combine the eight RF RX channels based on RX sensitivities measured in a pre-scan, yielding a TRX phase as if the body coil would have been used both for TX and RX. If no such option is available at the scanner applied, RF RX channels can be combined in a post-processing step, e.g., as it is done for parallel imaging [34] with reduction factor R = 1, using separately measured RX sensitivities. A detailed description of RF coil combination for EPT is given by [22, 24]. B_1 phase maps of example slices for both, phantom and in vivo, are shown in Fig. 8.1b, e. The phase jump of 180° occurring in the oil compartment has been compensated offline to better visualize spatial phase distribution.

8.4 MREPT Image Reconstruction

8.4.1 Physical Background

This section outlines the physical and mathematical background of EPT. More details are given in corresponding reviews [16, 27]. For beginners

it is recommended to start EPT with its most simplified version, which is

$$\sigma = \frac{\nabla^2 \phi}{\omega \mu_0} \tag{8.3}$$

The essential message of this equation is that conductivity σ is proportional to the curvature of the B_1-phase ϕ. The measurement of ϕ is described in Sect. 8.3.2, and the calculation of curvature numerically is described in a post-processing step in Sect. 8.4.2 below. The curvature is obtained by the second derivative in all three spatial dimensions, given by ∇^2 in (8.3). The Larmor frequency ω and the vacuum permeability μ_0 (assumed to be constant) act as scaling factors to convert the phase curvature to quantitative conductivity values with the SI unit (S/m). Thus, in this simplest form, no iteration, matrix inversion, or other "advanced" numerical method is required for EPT, and conductivity can be calculated (semi-) locally in a straightforward manner.

As next step, to calculate not only conductivity but also permittivity, a complex version of (8.3) is needed (sometimes called "truncated" Helmholtz equation)"

$$\kappa = \omega\varepsilon - i\sigma = -\frac{\nabla^2 B_1^+}{\omega \mu_0 B_1^+} \tag{8.4}$$

The real part of (8.4) comprises permittivity; the imaginary part comprises conductivity. Equation (8.4) is accurate assuming that electrical properties κ are locally constant, i.e., $\nabla\kappa = 0$ (the so-called local homogeneity assumption, LHA). If the LHA is not fulfilled, the equation gets more complicated, yielding "full" Helmholtz equation:

$$\kappa \mathbf{B_1} = -\frac{\nabla^2 \mathbf{B_1}}{\omega \mu_0} - \frac{(\nabla\kappa/\kappa) \times (\nabla \times \mathbf{B_1})}{\omega \mu_0} \tag{8.5}$$

Comparing Eqs. (8.4) and (8.5), we can notice that the Eq. (8.5) requires not only the introduction of an additional term on the right hand side, to handle the local inhomogeneity of κ, but also the transition to a vector equation. Note that the vector $\mathbf{B_1} = \left[B_{1x}, B_{1y}, B_{1z}\right]$ describes the RF coil's full magnetic field instead of the previously used scalar B_1^+ (the positive circularly polarized component of $\mathbf{B_1}$; see below). Equation (8.5), which involves only $\mathbf{B_1}$, can be derived by taking the curl of both sides of the Ampere's law with Maxwell's correction ($\nabla \times \mathbf{B_1} = i\mu_0\kappa\mathbf{E}$) and then combining it with Faraday's law from Maxwell's equations ($\nabla \times \mathbf{E} = -i\omega\mathbf{B_1}$) assuming time-harmonic fields. Gurler et al. [7] have shown that for $\sigma^2 \gg (\omega\varepsilon)^2$, Eq. (8.5) can be transformed into the transceive phase-based EPT equation as

$$(\nabla\sigma/\sigma) \cdot \nabla\phi^{tr} - \nabla^2\phi^{tr} + 2\omega\mu_0\sigma = 0 \tag{8.6}$$

As mentioned above, a standard MR system allows only the measurement of the so-called transceive (TRX) phase, which is the superposition of RF TX phase and RF RX phase. The TX phase required for the Eq. (8.6) above can be estimated by scaling the measured TRX phase ϕ_{tr} by a factor 1/2 assuming that TX and RX phase are equal (so-called "TRX Phase Assumption," TPA). Before doing so, care has to be taken that the measured phase is correctly unwrapped. Fortunately, phase unwrapping does not need to be 3D (a rather nontrivial task) but could be 1D (a rather trivial task) performed separately for each spatial direction—in connection with the numerical differentiation, which can also be performed in each spatial direction separately (see below). Doing this scaling of $\phi = \phi_{tr}/2$ will provide us the following equation:

$$\sigma = \frac{\nabla^2\phi}{\omega\mu_0} - \frac{(\nabla\sigma/\sigma) \cdot \nabla\phi}{\omega\mu_0} \tag{8.7}$$

Equation (8.7) is in the form of a convection-reaction equation and thus dubbed cr-EPT. For a locally constant σ, $\nabla\sigma = 0$, and therefore Eq. (8.7) reduces to Eq. (8.3).

Complex Components of B_1

MR measurements of $\mathbf{B_1}$, B_1^+, or even ϕ are challenging. The longitudinal component B_{1z} is generally not measurable, but for the usually applied RF quadrature volume

(continued)

coils, this is much smaller than B_{1x} and B_{1y} and is thus frequently neglected. The transverse components B_{1x} and B_{1y} could be derived from the positive $(B_{1x}+iB_{1y})/2$ and negative $(B_{1x}-iB_{1y})/2$ circularly polarized components, related to the TX and RX field of an RF coil, respectively. However, MRI allows only the magnitude of the TX field B_1^+ to be measured exactly, e.g., by methods presented in the Sect. 8.3 above, thus asking for further model assumptions to solve Eq. (8.5) [7, 25] and bring it in the form of Eq. (8.7). Note that $|B_1^+|$ is referred to as B_1 in Sect. 8.2.

8.4.2 Numerics

Most EPT reconstruction techniques, particularly the standard EPT reconstruction technique for beginners, are based on numerical differentiation, first and foremost by applying Eq. (8.3) for post-processing of measured TRX phase maps. However, numerical differentiation has a strong noise-amplifying effect, and that is why EPT reconstructions typically consist of two steps, differentiation and denoising. Thus, denoising filters for EPT should not be considered as cosmetic operations to improve some awkward reconstruction results but as an inherently required reconstruction step. Of course there are countless techniques published for both numerical differentiation and denoising. This chapter focusses on the description of techniques which are (a) easy to implement and (b) already applied in the framework of EPT.

Numerical Differentiation

It is impossible to perform numerical differentiation on a single voxel. Instead, to obtain the derivative of a certain voxel (the "target voxel"), a number of voxels around the target voxel are required (the "kernel"). The derivative is obtained by summing up all voxels of the kernel using suitable weighting coefficients D_n. The optimum choice of D_n leads to an intricate discussion but always starts with the simplest choice, which is determined starting with

$$\frac{\partial\phi}{\partial r} \approx \frac{\Delta\phi}{\Delta r} = \frac{\phi_{n+1}-\phi_n}{\Delta r} \tag{8.8}$$

as first derivative of ϕ with respect to r (r representing an arbitrary spatial direction). This equation replaces the infinitesimal differentiation operation ∂ by finite differences Δ, and these finite differences correspond to differences of neighbor voxels $n+1$ and n. The neighbor voxels have a distance Δr, which is the same as the voxel size in this direction. Continuing this way to the second derivative as required by Eq. (8.3) yields

$$\frac{\partial^2\phi}{\partial r^2} \approx \frac{\frac{\phi_{n+1}-\phi_n}{\Delta r} - \frac{\phi_n-\phi_{n-1}}{\Delta r}}{\Delta r} = \frac{\phi_{n+1}-2\phi_n+\phi_{n-1}}{(\Delta r)^2} \tag{8.9}$$

i.e., the same technique as before applied to two neighbor voxels of the first derivative. Voxel n is the target voxel, and the kernel consists of three voxels n, $n-1$, and $n+1$. The weighting coefficients for these three voxels are $D_n = \{+1,-2,+1\}$ as taken from the numerator of the right hand side of (8.9), yielding the simplest choice of weighting coefficients. It can be easily checked for the example phase of $\phi_n = n^2$ that (8.9) yields the desired curvature of $(1\cdot 1^2 - 2\cdot 0^2 + 1\cdot 1^2)/1^2 = 2$ (at $n=0$) or, as equivalent example, $(1\cdot(-3)^2 - 2\cdot(-2)^2 + 1\cdot(-1)^2)/1^2 = 2$ (at $n=-2$). The transition from the 1D case given in (8.9) to the 3D case as required by (8.3) is a trivial step, since (8.9) can be applied just thrice, once for each spatial direction x, y, and z, and the results added.

For a noiseless situation, as usually delivered by electromagnetic field simulation

(continued)

software, (8.9) yields rather perfect results (at least with sufficiently small voxel size and within areas of homogeneous electric properties). The situation gets complicated with the onset of noise in the measured ϕ (or artificial noise added to the simulation result), which is strongly amplified by (8.9). Although denoising is typically performed in a separate step (see below "Local Denoising"), noise can additionally be treated by increasing the numerical differentiation kernel, with weights optimized for denoising. The drawback of this concept is a loss of spatial resolution, i.e., increasing kernel size lowers noise and spatial resolution of the resulting conductivity map, just as would happen by choosing larger voxels for measurement. Thus, a suitable trade-off for the kernel size has to be found, which depends on the SNR of the measured image. The complexity of this discussion is demonstrated in [20]. A typical trade-off might be a kernel size of 11 voxels per direction, with weighting coefficients designed to fit a parabola to the voxels, as is given by Savitzky and Golay [36] and is thus usually called Savitzky-Golay coefficients:

$$D_n = \{+15, +6, -1, -6, -9, -10, -9, -6, -1, +6, +15\}/429. \tag{8.10}$$

Interestingly, these coefficients itself have the shape of a parabola. Savitzky-Golay coefficients for other kernel size are described in [36]. The minimum Savitzky-Golay kernel has a size of three coefficients and coincides with (8.9).

Numerical Denoising

Numerical denoising is typically performed after the differentiation step. Attempts of denoising before the differentiation step [30] might be hampered by the intrinsic feature of the B_1 magnitude and phase of being nonconstant, whereas electrical properties tend to be approximately constant over each tissue type, and constant quantities are easier to denoise than nonconstant quantities. Again, numerical denoising is a very large field, and this subsection sketches only two filter types most simple and applied in EPT community: the Gaussian filter and the median filter. As for numerical differentiation, denoising is always based on an ensemble of voxels around the target voxel, thus now leading to the "filter kernel." The geometric size and shape of the filter kernel might coincide with the differentiation kernel, but not necessarily. The Gaussian filter obtains its weighting coefficients F_n from a Gauss function

$$F_n = \exp(-a(n - n_0)^2) \tag{8.11}$$

with its maximum located at the target voxel n_0. The width of the Gauss function is determined by the parameter a, which can be chosen freely and distinguishes strong filtering (small a, i.e., broad exponential function) from weak filtering (large a, i.e., narrow/peaked exponential function). For large a, it does not make sense to use a very large kernel size as most of the weighting coefficients might be close to zero anyway. For small a, the kernel size has a big impact on the strength of the filter. The Gaussian filter is a "classical" filter which not only denoises but also blurs the image and is again to some extent equivalent with using larger voxels during acquisition. The median filter is slightly less simple than the Gaussian filter but typically yields more "realistic" results than the Gaussian filter, tending to preserve edges instead of blurring them. In a first step, the median filter creates a histogram of the kernel's values. In contrast to a standard histogram,

(continued)

it is advantageous to choose the bins of the histogram so small that all bins contain only one or zero voxels. In a second step, the filter identifies the histogram's median value as 50% of the voxels above and 50% below this value. This median value is then assigned to the corresponding target voxel of the denoised image. The median filter does not include free parameters in contrast to the Gauss filter (having freely adjustable parameter a).

Local Adaptation of Kernel Shape

As outlined above, Eqs. (8.3) and (8.4) are based on the local homogeneity assumption, LHA. This LHA is most often violated at boundaries separating tissues with differing electrical properties, and due to the finite size of differentiation and filter kernel, it is also violated if these tissue boundaries are somewhere inside the kernel. This is the reason why both, differentiation and filter kernel, should be shaped such that they never cross tissue boundaries. In other words, for each target voxel, the kernel should contain only voxels which belong to the same tissue type as the target voxel. This is relatively straightforward to implement and supersedes the much more sophisticated implementation of (8.3) and (8.4) having the same goal: to overcome the EPT boundary problem.

To shape the differentiation and filter kernel locally to the individual tissue boundaries, the magnitude image can be taken into account, which is acquired together with the transceive phase (i.e., typically a SE-based or SSFP image, see Sect. 8.3.2 above). The easiest way to take this magnitude image into account is to compare the signal of the target voxel with the signal of the (potential) kernel voxel. Thus, a maximum kernel size is defined, and within this maximum kernel, all voxels n are skipped which signals' $S(n)$ differ from the target voxel's signal $S(n_0)$ by more than a predefined threshold R_{thresh} [17]:

$$|S(n)/S(n_0) - 1| > R_{thresh} \qquad (8.12)$$

A related strategy is to apply an edge detection filter to the magnitude image and to iteratively increase the kernel from the target voxel up to the surrounding edges [13].

It should be noted that boundary artifacts have two origins, a physical and a numerical [28]. The physical artifact is caused by the missing term in (8.4) and can be removed by using (8.5), which includes the missing term. The numerical artifact is caused by the discontinuity in the phase or in its first derivative, which is *not* removed using (8.4) but using (8.5). However, both types of boundary artifacts are removed by the described local shaping of differentiation and filter kernel.

8.4.3 Advanced EPT Reconstruction Techniques

MREPT clinical studies have recently started appearing in some research works such as the breast cancer study reported by Shin et al. [38] and the brain tumor study reported by Tha et al. [40]. Notably, the EPs reconstructed in these studies are based on Eq. (8.3) using numerical differentiation, which indicates that even the simplest possible version of EPT is able to yield meaningful clinical results. Nevertheless, researchers are attempting to improve EPT by developing more advanced reconstruction techniques. A big step toward more advanced EPT reconstruction techniques is to replace Eqs. (8.3) and (8.4) by Eqs. (8.5) and (8.7) for better handling of the EPT boundary problem. As mentioned earlier, this strategy has been chosen

for "gradient EPT" [25] or "convection-reaction EPT" [7,8,10]. These techniques however are still based on numerical differentiation. Methods have also been developed to overcome the need for numerical differentiation. Some of these methods are summarized in this section. These methods belong to the family of forward reconstructions and machine learning reconstructions.

Forward Reconstruction

Standard EPT can be considered as a "backward" solution: a measured B_1 (or its phase ϕ) is taken and post-processed to get back to the underlying electrical properties. In contrast, "forward" solutions start with an assumed distribution of electrical properties (assumed patient tissue structure), then simulates the resulting B_1, and compares the simulated and measured B_1. Typically, this yields an iterative process, which optimizes the assumed input electrical properties until difference between the simulated, and the measured B_1 is minimized (method pioneered by Balidemaj et al. [3] as "contrast source inversion" EPT (CSI-EPT). No differentiation or denoising is required for such forward solutions, which can be regarded as advantage of this method. Instead, two reconstruction steps are applied: the forward simulation of the B_1 field (e.g., including the question of how far the knowledge of the applied RF coil and its shield is required for this goal [2]) and the iteration of the input electrical properties (e.g., including the question of optimal initial iteration [23]). However, since there is requirement of iterative steps for reconstruction, this can easily exceed the complexity and the CPU time required for reconstruction with "forward" EPT compared to the "backward" EPT.

Machine Learning Reconstruction

First steps have been undertaken to test the ability of EPT for machine learning, which is another way to circumvent differentiation and denoising required by Eqs. (8.3), (8.4), (8.5), and (8.7). The main challenge in this context is to provide sufficient ground truth, i.e., a multitude of examples connecting B_1 field and electrical properties. In a first attempt, ground truth was provided by a dictionary containing small patches of B_1 fields together with underlying electrical properties, taken from electromagnetic simulations of homogeneous spheres [11]. More advanced, neural networks have been applied to learn the connection between B_1 fields and electrical properties, as provided by 2D brain simulations and applied to measured B_1 fields [29]. As is always the case, a lengthy learning process is required for the network, allowing for very fast reconstruction of the individually measured patient. Again, as is always the case, generalization might be an issue, i.e., how much a measured B_1 field is allowed to differ from the training data and still having a chance to be reconstructed reliably. Generalization of course improves with the variety of ground truth data, but one has to keep in mind that simulating B_1 fields from assumed tissue structures is a rather time-consuming procedure (see above "Forward Reconstruction").

8.4.4 Permittivity Reconstruction

Continuing to more advanced reconstruction methods, it might become possible to obtain not only satisfying conductivity results but also satisfying permittivity results. Permittivity is much less considered in EPT studies than conductivity. This is not only due to the less known meaning of this parameter (particularly among clinicians) but also because it is discriminated by underlying physics to be less sensitive for B_1 measurements and, thus, even more prone to low SNR than conductivity. Studies suggest that with standard EPT, satisfying in vivo

permittivity results cannot be expected below a main field strength of 7T [42]; however, this might change for advanced versions of EPT.

8.5 MREPT Experiments

8.5.1 Phantom Experiment

It is very simple to build a phantom which fulfils basic requirements to start with EPT. In short, roughly half of a bottle is filled with saline in a first step, and in a second step, oil is added to the saline until the bottle is filled, yielding a phantom with two compartments. The oil will always swim on the saline; thus a sharp boundary between the compartments is guaranteed (without any unwanted vessel wall, foil, or the like separating the two compartments). Furthermore, a conductivity contrast is guaranteed, since oil has typically a very low conductivity (close to zero), and saline has a conductivity significantly different from zero. All required substances are harmless, cheap, and stable. Some more details are given in the following sections.

The Bottle In principle, any bottle or vessel can be used, as long as it does not contain any metallic material (i.e., preferably made from plastic or glass), can be closed tightly (watch out for leaking oil/saline), and fits into the receive RF (head) coil used for MRI data acquisition. In fact, it should be as large as possible to permit high SNR by enabling a large voxel size.

The Saline For simple initial experiments, just tap water can be used with standard table salt (sodium chloride, NaCl) added. A conductivity σ should be adjusted which is somewhat high but yet reasonably within the physiologic range, for instance $\sigma \approx 1$ S/m. This value corresponds to roughly 6.5 g NaCl per liter H_2O (about a "teaspoon of salt"). For more precise quantities of NaCl and its relation with conductivity, see Chap. 2 (MREIT Phantoms).

The Oil For simple initial experiments, some standard oil for cooking from the supermarket is sufficient (e.g., rape oil, sunflower oil, olive oil). All these types of oil have the two necessary features, i.e., swimming on water and conductivity of approximately zero; thus the cheapest (and/or scentless) oil available might be taken. Pouring the oil onto the water might lead to small bubbles at the oil/water interface, which typically dissolve within a few hours without further interaction.

MRI of the Phantom
In principle, contrast agent might be used for this phantom, but is not mandatory. Both saline and oil might show suboptimal signal, but sufficient SNR could be achieved by reasonable voxel size and number of averages. The use of contrast agent might be tricky since (a) it usually changes conductivity, and (b) it might be soluble only in water (saline) but not in oil, thus leading to a nasty huge signal difference between the compartments. A picture of such a phantom is shown in Fig. 8.2, and corresponding MR images are shown in Fig. 8.1a–c.

8.5.2 In Vivo Human Experiment

It is straightforward to perform initial in vivo EPT experiments. First, a healthy subject willing to volunteer is required, and approval of the corresponding local Institutional Review Board (IRB) (or Ethics Committee) has to be obtained. It is strongly recommended to start with imaging the brain of the volunteer, which is the part of the body with the lowest motion, sufficiently high structural contrast, and no problems with water/-fat chemical shift. Using the sequence discussed below, SNR in the brain is large enough to perform the EPT experiment within a few minutes, which is a duration for which all healthy subjects are easily able to keep still. MR images of such an in vivo experiment are shown in Fig. 8.1d–f.

The literature electrical properties of brain tissue [5] at 128 MHz (i.e., Larmor frequency at B_0 = 3T) are given in Table 8.1 below. Conductivity of grey and white matter are within the typical range of around 0.5 S/m of all tissue types which

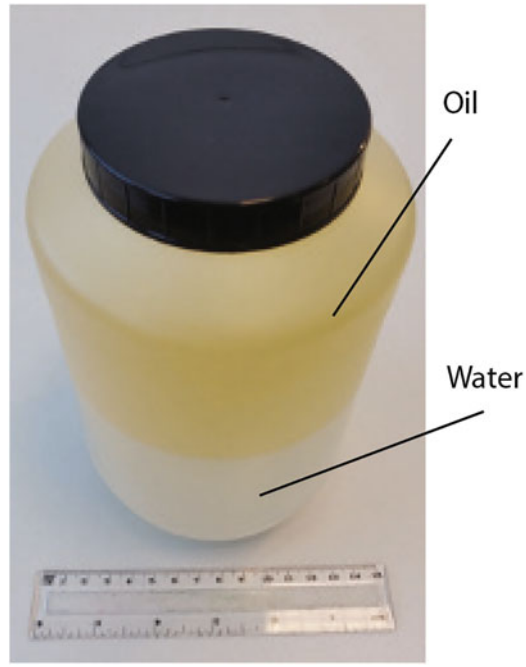

Fig. 8.2 Photo of phantom with two compartments. Upper compartment, rape oil; lower compartment, saline. The bottle has a diameter of roughly 12 cm and a height of roughly 15 cm

Table 8.1 Electrical properties of brain tissue types at 128 MHz according to [5]

	Grey matter (GM)	White matter (WM)	Cerebrospinal fluid (CSF)
Conductivity (S/m)	0.59	0.34	2.14
Permittivity ($/\varepsilon_0$)	73.5	52.5	84.0

are not fluids (high conductivity) or fat or bone (both low conductivity). In fact, CSF has the highest tissue conductivity reported, even higher than all other body fluids typically in the range 1.0–1.5 S/m. Similarly, permittivity of CSF is the highest one reported, close to the maximum permittivity of water. Grey and white matter are in an intermediate range, and fat and bone are at the lower end of the tissue permittivity range [5].

The only issue connected with EPT brain imaging is cardiac pulsation transferred to cerebrospinal fluid (CSF) [18]. Without pulsation, the conductivity of CSF is quite high compared to surrounding gray/white matter (GM/WM), thus yielding a clearly visible conductivity contrast as outlined above. However, with pulsation, roughly 50% of scans show a corrupted CSF conductivity, depending on the incidental distribution of k-space acquisition in relation to cardiac cycle. Cardiac triggering does not help in this situation, since optimal point in time in cardiac cycle for EPT acquisition is different for different parts of the brain (due to traveling of pulsation wave throughout brain over cardiac cycle). Corrupted CSF conductivity is hardly a problem since clinicians are usually not interested in CSF conductivity. However, if a "nice" conductivity map free of CSF pulsation artifacts is desired, the easiest way is to repeat the measurement a couple of times and check for conductivity map with lowest amount of pulsation artifacts.

8.5.3 Examples of Phantom/In Vivo Reconstructions

Phantom Reconstructions

Different reconstruction examples of phantom conductivity are shown in Fig. 8.3. Us-

(continued)

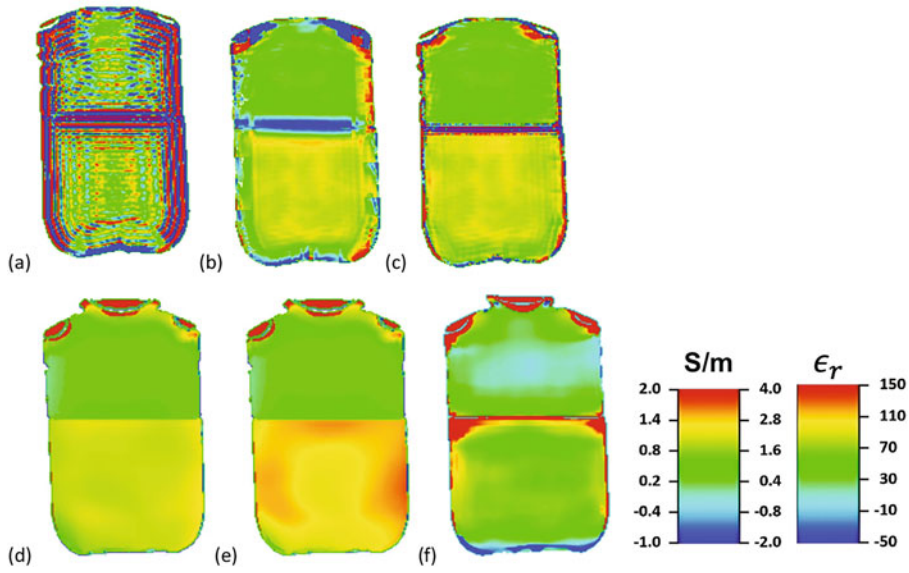

Fig. 8.3 Different reconstruction examples of phantom conductivity. Numbers on the right hand side of the conductivity color scale apply to (**a**) and numbers on the left-hand side to (**b**)–(**e**). (**a**) Reconstruction using a small differentiation kernel, conductivity appears noisy and with strong ripples. (**b**) Reconstruction with a larger kernel removes noise and ripples but yields a strong artifact along the compartment boundary. (**c**) Reconstruction taking compartment boundaries into account reduces the boundary artifact. (**d**) Reconstruction including a median filter removes most of the remaining noise and ripples in part (**c**). (**e**) Reconstruction assuming a constant B_1 magnitude, i.e., a purely phase-based reconstruction using (8.3). (**f**) Relative permittivity, corresponding to reconstruction of (**d**)

ing a small differentiation kernel of three voxels, reconstructed conductivity appears noisy and with strong ripples as is visible in Fig. 8.3a. Please note that color scale of Fig. 8.3a is twice the color scale of the remaining subplots to better visualize the effects. The larger kernel of 11 voxels from Eq. (8.10) removes noise and ripples but yields a strong artifact (over/undershoot) along the compartment boundary, as is visible from Fig. 8.3b. Taking compartment boundaries into account during differentiation via Eq. (8.12) greatly reduces this artifact (Fig. 8.3c). The median filter, again using (8.12), removes most of the remaining noise and ripples (Fig. 8.3d). If B_1 magnitude is ignored by assuming a constant B_1 magnitude (i.e., using Eq. (8.3) instead of (8.7)), saline compartment shows a ring-shaped increase of conductivity (Fig. 8.3e). This increase corresponds to areas with strong gradients of the B_1 magnitude, as visible on Fig. 8.1c. Since in the oil compartment, B_1 magnitude is rather flat anyway, no significant difference is observed in this compartment between Fig. 8.1d, e. Reconstructed permittivity suffers from more artefacts than conductivity, but the permittivity difference between oil and saline is clearly visible in Fig. 8.3f.

In Vivo Reconstructions in the Human Brain

In analogy to the phantom results shown in Fig. 8.3, different reconstruction examples of in vivo brain conductivity are shown in Fig. 8.4. Using again the small differentiation kernel of three voxels, reconstructed

(continued)

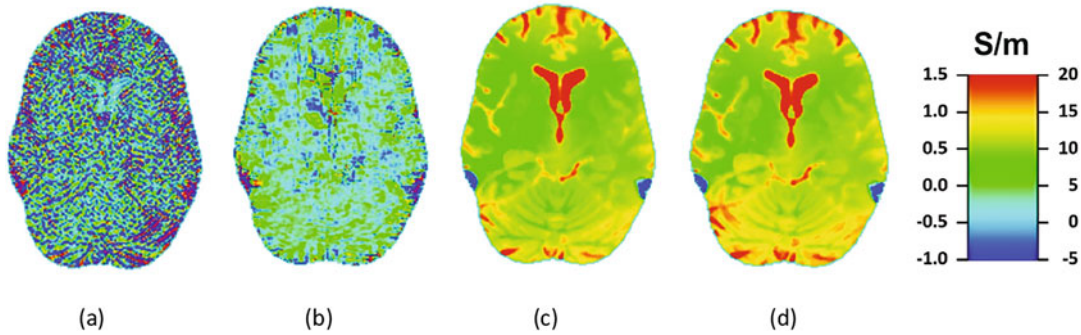

Fig. 8.4 Different reconstruction examples of brain conductivity. Numbers on the right hand side of the color scale apply to (**a**)–(**b**) and numbers on the left-hand side to (**c**)–(**d**). (**a**) Reconstruction using a small differentiation kernel, conductivity appears noisy and with strong ripples. (**b**) Reconstruction with a larger kernel reduces noise and ripples. (**c**) Reconstruction taking compartment boundaries and a median filter into account essentially removes noise and ripples. (**d**) Reconstruction assuming a constant B_1 magnitude, i.e., a purely phase-based reconstruction using (8.3)

conductivity appears noisy and with strong ripples (Fig. 8.4a). Please note that again different color scales have been applied for the different subplots to better visualize the effects. The larger kernel of 11 voxels reduces noise and ripples (Fig. 8.4b). Taking into account a median filter and compartment boundaries, via Eq. (8.12), greatly reduces noise and ripples (Fig. 8.4c). If the effect of B_1 magnitude is ignored by assuming a constant B_1 magnitude (i.e., using (8.3) instead of (8.7)), a slight increase of conductivity appears toward the rim of the brain (visible by increased appearance of orange and red areas). As for the phantom, this increase corresponds to gradients of the B_1 magnitude, as visible on Fig. 8.1f. Small banding artifacts are visible in the lower left and right, arising from air cavities in the ears, leading to nonphysical ("blue") negative conductivity in these areas.

Inference from Phantom and In Vivo Experiments

The results allow the conclusion that although conductivity is encoded in the B_1 phase, it is usually not obvious by visual inspection of the phase, particularly in vivo. The specific setup of the phantom enables our eyes to distinguish a flat phase in the oil compartment from the curved phase in the saline compartment. This is no longer the case for in vivo: here, a global phase curvature across the brain is visible, but different local curvature according to anatomic details cannot be distinguished by our sight.

8.5.4 Preclinical Experiments

Various preclinical EPT studies have been performed in the recent years, predominantly on rodent models. According to the human studies conducted, the preclinical studies investigated mainly tumors models [12, 24, 26, 32, 43] but also stroke models [1, 14, 19]. An exemplary result for a rat tumor model [24] is shown in Fig. 8.5, reporting conductivity values increasing linearly with tumor growth, while diffusion values do not change with tumor growth. This study has been performed at 9.4T, representative for the trend toward high field strength for preclinical studies (up to 21.1T applied in [1]), but standard clinical field strength does not prohibit preclinical EPT studies (e.g., [14, 32]). While brain mapping appears to

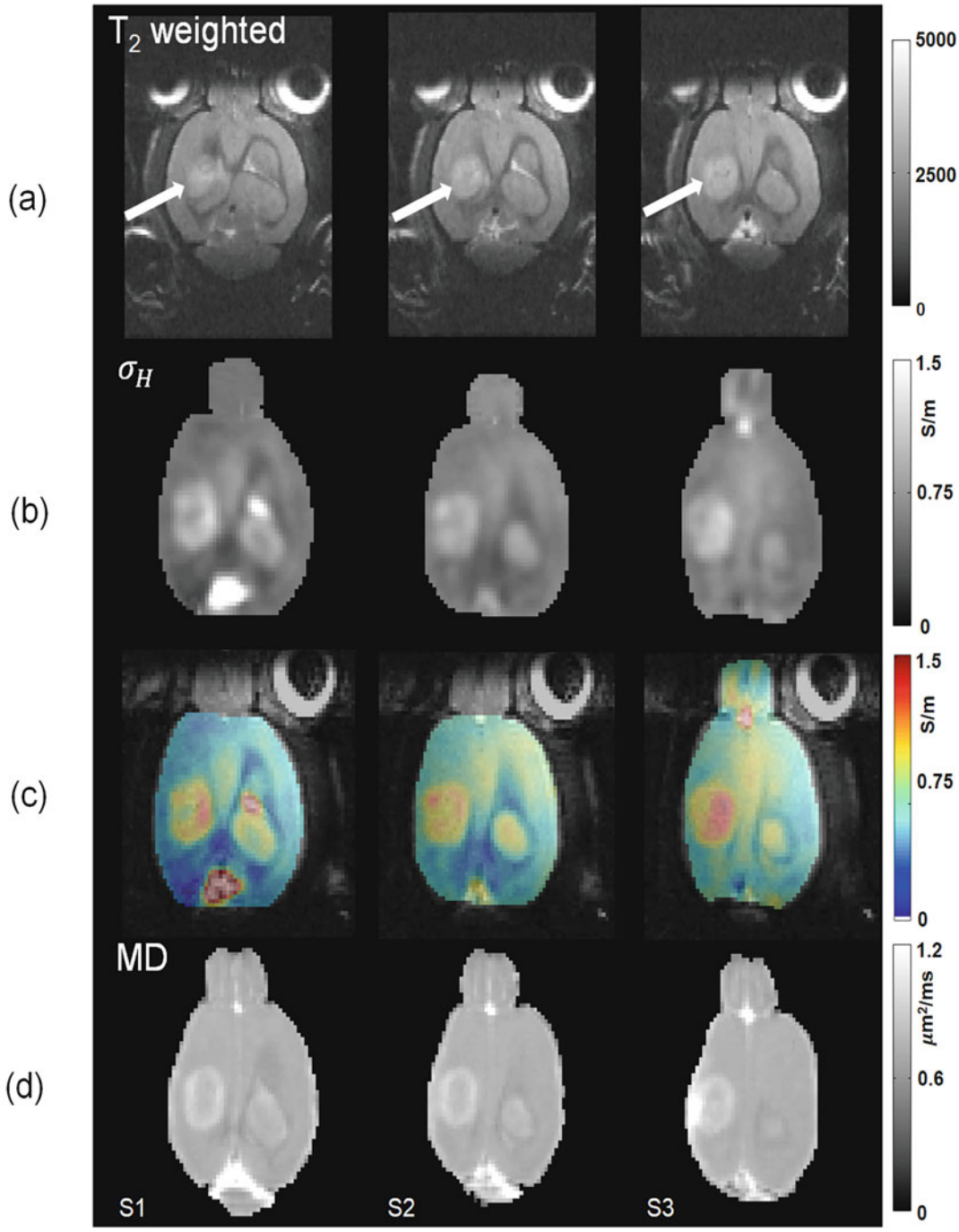

Fig. 8.5 Example of preclinical experiment [24]. F98 rat brain tumor images for three slices S1, S2, S3 showing the widest spread of the tumor growth in the brain of this rat. (**a**) T2-weighted images, (**b**) high-frequency conductivity images at 400 MHz, (**c**) conductivity images in (**c**) overlayed over the images in (**a**), and (**d**) mean diffusivity (MD) images

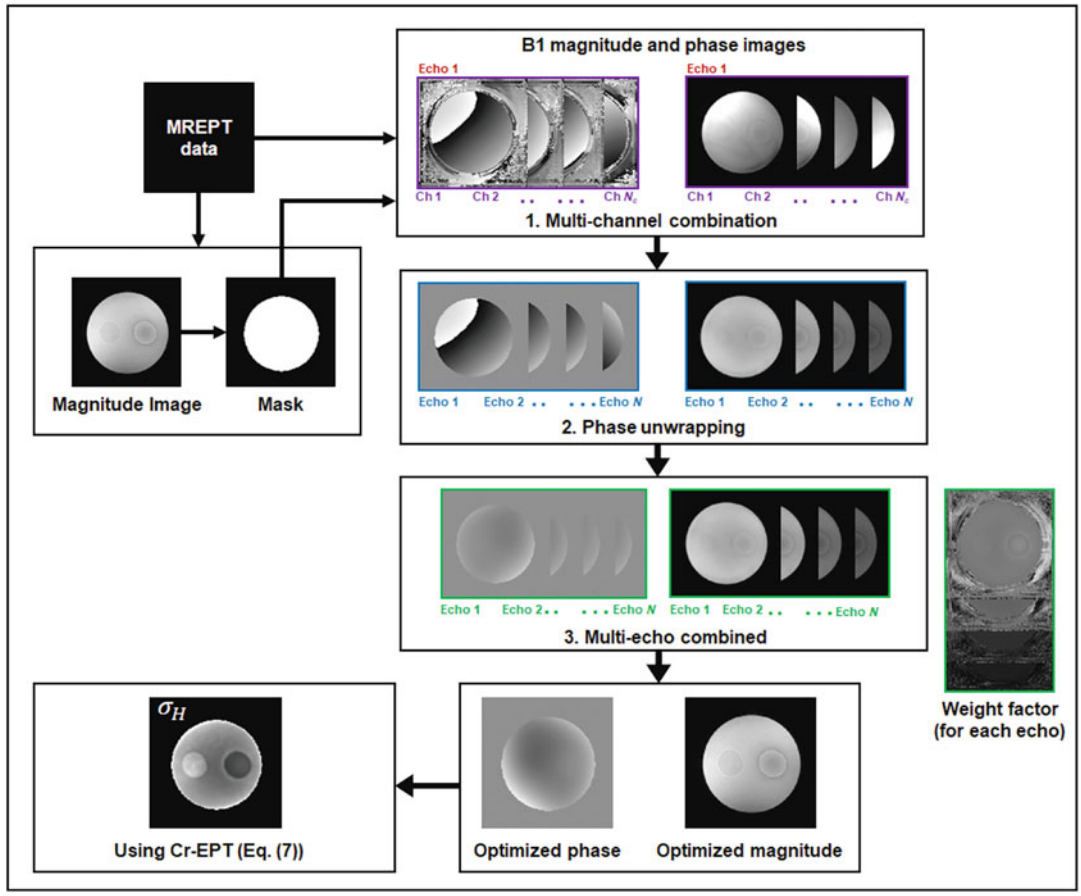

Fig. 8.6 Example of EPT workflow in case that multiple echoes have been acquired with multiple RF RX coils. Starting from the upper left, the pre-processing steps required to combine the multichannel and multi-echo data acquired with multi-echo spin/gradient echo pulse sequences are depicted, eventually leading to the final reconstruction result (lower left)

be the most promising application of EPT, cardiac EPT is obviously one of the most challenging applications, and only a single cardiac animal study has been published yet (reporting a decreased conductivity in the infarcted area [44]).

Appendix

When single echo pulse sequences are used in phase-based EPT, the $\mathbf{B_1}$ phase calculation is straightforward. However, when multi-echo pulse sequences are used with multichannel receive RF coils, the phase calculation becomes complicated. While various methods are developed for combination of channels and echoes to create one phase image per slice, they all have some generic steps. These steps are demonstrated using a cylindrical shaped phantom with two cylindrical anomalies in Fig. 8.6. Note that the background voxels of conductivity images are generally removed by segmenting the masks from magnitude images. This is illustrated in Fig. 8.6 and the effect of using mask is evident in Fig. 8.5b and (c) images.

References

1. G. Amouzandeh, F. Mentink-Vigier, S. Helsper, F.A. Bagdasarian, J.T. Rosenberg, S. Grant, Magnetic resonance electrical property mapping at 21.1 T: a study

of conductivity and permittivity in phantoms, ex vivo tissue and in vivo ischemia. Phys. Med. Biol. **65**, 055007 (2019)
2. A. Arduino, L. Zilberti, M. Chiampi, O. Bottauscio, CSI-EPT in presence of RF-shield for MR-coils. IEEE Trans. Med. Imag. **36**, 1396–1404 (2017)
3. E. Balidemaj, C.A. van den Berg, J. Trinks, A.L. van Lier, A.J. Nederveen, L.J. Stalpers, H. Crezee, R.F. Remis, CSI-EPT: a contrast source inversion approach for improved MRI-based electric properties tomography. IEEE Trans. Med. Imag. **34**, 1788–96 (2015)
4. N. Choi, M. Ghim, S. Yang, S.Y. Zho, D.H. Kim, In vivo conductivity mapping using double spin echo for flow effect removal, in *Proceedings of the 19th Annual Meeting of the ISMRM* (ISMRM, Concord, 2011), p. 4466
5. C. Gabriel, S. Gabriel, E. Corthout, The dielectric properties of biological tissues: I. Literature survey. Phys. Med. Biol. **41**, 2231–2249 (1996)
6. S. Gavazzi, C.A.T. van den Berg, A. Sbrizzi, H.P. Kok, L.J.A. Stalpers, J.J.W. Lagendijk, H. Crezee, A.L.H. van Lier, Accuracy and precision of electrical permittivity mapping at 3T: the impact of three B1 mapping techniques. Magn. Reson. Med. **81**, 3628–3642 (2019)
7. N. Gurler, Y.Z. Ider, Gradient-based electrical conductivity imaging using mr phase. Magn. Reson. Med. **77**(1), 137–150 (2017)
8. N. Gurler, O.M. Oran, H.D. Keklikoglu, Y.Z. Ider, Application of generalized phase based electrical conductivity imaging in the subacute stage of hemorrhagic and ischemic strokes, in *Proceedings of the 24th Annual Meeting of the ISMRM*, p. 2994 (ISMRM, Concord, 2016)
9. E.M. Haacke, L.S. Pepropoulos, E.W. Nilges, D.H. Wu, Extraction of conductivity and permittivity using magnetic resonance imaging. Phys. Med. Biol. **36**, 723–734 (1991)
10. F.S. Hafalir, O.F. Oran, N. Gurler, Y.Z. Ider, Convection-reaction equation based magnetic resonance electrical properties tomography (cr-mrept). IEEE Trans. Med. Imag. **33**(3), 777–793 (2014)
11. N. Hampe, M. Herrmann, T. Amthor, C. Findeklee, M. Doneva, U. Katscher, Dictionary-based electric properties tomography. Magn. Reson. Med. **81**, 342–349 (2019)
12. I. Hancu, J.C. Roberts, S. Bulumulla, S.K. Lee, On conductivity, permittivity, apparent diffusion coefficient, and their usefulness as cancer markers at MRI frequencies. Magn. Reson. Med. **73**, 2025–2029 (2015)
13. L. Huang, F. Schweser, K.H. Herrmann, M. Krämer, A. Deistung, J.R. Reichenbach, A Monte Carlo method for overcoming the edge artifacts in MRI-based electrical conductivity mapping, in *Proceedings of the 22nd Annual Meeting of the ISMRM* (ISMRM, 2014), p. 3190
14. U. Jensen-Kondering, L. Shu, R. Böhm, O. Jansen, In-vivo pilot study at 3 tesla: feasibility of electric properties tomography in a rat model of stroke. Phys. Med. **9**, 100024 (2020)
15. U. Katscher, P. Börnert, Imaging of lung conductivity using ultrashort echo-time imaging, in *Proceedings of the 24th Annual Meeting of the ISMRM* (ISMRM, 2016), p. 2923
16. U. Katscher, C.A.T. van den Berg, Electric properties tomography: biochemical, physical and technical background, evaluation and clinical applications. NMR Biomed. **30**, 3729 (2017)
17. U. Katscher, K. Djamshidi, T. Voigt, M. Ivancevic, H. Abe, G. Newstead, J. Keupp, Estimation of breast tumor conductivity using parabolic phase fitting, in *Proceedings of the 20th Annual Meeting of the ISMRM* (ISMRM, 2012), p. 3482
18. U. Katscher, C.H. Stehning, K.K. Tha, The impact of CSF pulsation on reconstructed brain conductivity, in *Proceedings of the 26th Annual Meeting of the ISMRM* (ISMRM, 2018), p. 546
19. D.H. Kim, M. Chauhan, M.O. Kim, W.C. Jeong, H.J. Kim, I. Sersa, O.I. Kwon, E.J. Woo, Frequency-dependent conductivity contrast for tissue characterization using a dual-frequency range conductivity mapping MR method. IEEE Trans. Med. Imag. **34**, 507–513 (2015)
20. S.K. Lee, S. Bulumulla, I. Hancu, Theoretical investigation of random noise-limited signal-to-noise ratio in MR-based electrical properties tomography. IEEE Trans. Med. Imag. **34**, 2220–2232 (2015)
21. S.K. Lee, S. Bulumulla, F. Wiesinger, L. Sacolick, W. Sun, I. Hancu, Tissue electrical property mapping from zero echo-time magnetic resonance imaging. IEEE Trans. Med. Imag. **34**, 541–550 (2015)
22. J.S. Lee, J.W. Shin, D.H. Kim, MR-based conductivity imaging using multiple receiver coils. Magn. Reson. Med. **76**, 530–539 (2016)
23. R. Leijsen, C.A.T. van den Berg, R. Remis, A. Webb, S. Mandija, Improving tissue electrical properties reconstructions by exploiting the benefits of combining deep learning-EPT and 3d contrast source inversion-EPT, in *Proceedings of the 27th Annual Meeting of the ISMRM* (ISMRM, 2019), p. 5050
24. C. Lesbats, N. Katoch, A.S. Minhas, A. Taylor, H.J. Kim, E.J. Woo, H. Poptani, High-frequency electrical properties tomography at 9.4t as a novel contrast mechanism for brain tumors. Magn. Reson. Med. **86**(1), 382–392 (2021)
25. J. Liu, X. Zhang, S. Schmitter, P.F. van de Moortele, B. He, Gradient-based electrical properties tomography (gEPT): a robust method for mapping electrical properties of biological tissues in vivo using magnetic resonance imaging. Magn. Reson. Med. **74**, 634–646 (2015)
26. J. Liu, Q. Shao, Y. Wang, G. Adriany, J. Bischof, P.F. van de Moortele, B. He, In vivo imaging of electrical properties of an animal tumor model with an 8-channel transceiver array at 7 T using electri-

cal properties tomography. Magn. Reson. Med. **78**, 2157–2169 (2017)
27. J. Liu, Y. Wang, U. Katscher, B. He, Electrical properties tomography based on B1 maps in MRI: principles, applications, and challenges. IEEE Trans. Biomed. Eng. **64**, 2515–2530 (2017)
28. S. Mandija, A. Sbrizzi, U. Katscher, P.R. Luijten, C.A.T. van den Berg, Error analysis of helmholtz-based MR-electrical properties tomography. Magn. Reson. Med. **80**, 90–100 (2018)
29. E.F. Mandija, S. Meliadò, N.R.F. Huttinga, P.R. Luijten, C.A.T. van den Berg, Opening a new window on MR-based electrical properties tomography with deep learning. Sci. Rep. **9**, 8895 (2019)
30. E. Michel, D. Hernandez, M.H. Cho, S.Y. Lee, Denoising of B1 field maps for noise-robust image reconstruction in electrical properties tomography. Med. Phys. **41**, 1–9 (2014)
31. K. Nehrke, P. Börnert, DREAM-A novel approach for robust, ultrafast, multislice b1 mapping. Magn. Reson. Med. **68**, 1517–1526 (2012)
32. J.A. Park, K.J. Kang, I.O. Ko, K.C. Lee, B.K. Choi, N. Katoch, J.W. Kim, H.J. Kim, O.I. Kwon, E.J. Woo, In vivo measurement of brain tissue response after irradiation: comparison of T2 relaxation, apparent diffusion coefficient, and electrical conductivity. IEEE Tran. Med. Imag. **38**, 2779–2784 (2019)
33. R. Pohmann, K. Scheffler, A theoretical and experimental comparison of different techniques for b_1 mapping at very high fields. NMR Biomed. **26**, 265–275 (2013)
34. K.P. Pruessmann, M. Weiger, M.B. Scheidegger, P. Boesiger, SENSE: sensitivity encoding for fast MRI. Magn. Reson. Med. **42**, 952–962 (1999)
35. L.I. Sacolick, F. Wiesinger, I. Hancu, M.W. Vogel, B1 mapping by Bloch-Siegert shift. Magn. Reson. Med. **63**, 1315–1322 (2010)
36. A. Savitzky, M.J.E. Golay, Smoothing and differentiation of data by simplified least squares procedures. Anal. Chem. **36**, 1627–1639 (1964)
37. F. Schweser, L. Huang, K.H. Herrmann, M. Krämer, A. Deistung, J.R. Reichenbach, Conductivity mappingusing ultrashort echo time (UTE) imaging, in *Proceedings of the 27th Annual Meeting of the ISMRM* (ISMRM, 2013), p. 4190
38. J.W. Shin, M.J. Kim, J.S. Lee, Initial study on in vivo conductivity mapping of breast cancer using MRI. Magn. Reson. Med. **42**, 371–378 (2015)
39. C. Stehning, T.R. Voigt, U. Katscher, Real-time conductivity mapping using balanced SSFP and phase-based reconstruction, in *Proceedings of the 19th Annual Meeting of the ISMRM* (ISMRM, 2011), p. 128
40. K.K. Tha, U. Katscher, S. Yamaguchi, C. Stehning, S. Terasaka, N. Fujima, K. Kudo, K. Kazumata, T. Yamamoto, M. Van Cauteren, H. Shirato, Noninvasive electrical conductivity measurement by MRI: a test of its validity and the electrical conductivity characteristics of glioma. Eur. Radiol. **28**, 348–355 (2018)
41. A.L.H. van Lier, D.O. Brunner, K.P Pruessmann et al., B1 phase mapping at 7T and its application for in vivo electrical conductivity mapping. Magn. Reson. Med. **67**, 552–561 (2012)
42. A.L.H. van Lier, A. Raaijmakers, T. Voigt, J.J. Lagendijk, U. Katscher, C.A.T. van den Berg, Electric properties tomography in the human brain at 1.5, 3, and 7 T: a comparison study. Magn. Reson. Med. **71**, 354–363 (2014)
43. P.P. Vasudevan, R. Aminzadeh, N. de Geeter, B. Descamps, L. Dupré, W. Joseph, R. van Holen, In vivo electrical conductivity imaging of animal tumor model at 7T using EPT, in *Proceedings of the 1st World Conference on Biomedical Applications of Electromagnetic Fields* (European Cooperation in Science and Technology, Brussels, 2018), pp. 1–2
44. T. Voigt, A. Schuster, M. Ishida, C. Stehning, A. Chiribiri, E. Nagel, T. Schaeffter, Conductivity imaging of an ischemic pig heart model using electric properties tomography, in *Proceedings of the 20th Annual Meeting of the ISMRM* (ISMRM, 2012), p. 3483
45. V.L. Yarnykh, Actual flip-angle imaging in the pulsed steady state: a method for rapid three-dimensional mapping of the transmitted radiofrequency field. Magn. Reson. Med. **57**, 192–200 (2007)